

## ORBITAL MOTION OF YOUNG BINARIES IN OPHIUCHUS AND UPPER CENTAURUS-LUPUS

G. H. SCHAEFER<sup>1</sup>, L. PRATO<sup>2</sup>, & M. SIMON<sup>3</sup>

<sup>1</sup>The CHARA Array of Georgia State University, Mount Wilson Observatory, Mount Wilson, CA 91023, USA (schaefer@chara-array.org)

<sup>2</sup>Lowell Observatory, 1400 West Mars Hill Road, Flagstaff, AZ 86001, USA

<sup>3</sup>Department of Physics and Astronomy, Stony Brook University, Stony Brook, NY 11794, USA

### ABSTRACT

We present measurements of the orbital positions and flux ratios of 17 binary and triple systems in the Ophiuchus star forming region and the Upper Centaurus-Lupus cluster based on adaptive optics imaging at the Keck Observatory. We report the detection of visual companions in MML 50 and MML 53 for the first time, as well as the possible detection of a third component in WSB 21. For six systems in our sample, our measurements provide a second orbital position following their initial discoveries over a decade ago. For eight systems with sufficient orbital coverage, we analyze the range of orbital solutions that fit the data. Ultimately, these observations will help provide the groundwork toward measuring precise masses for these pre-main sequence stars and understanding the distribution of orbital parameters in young multiple systems.

*Keywords:* binaries: visual, stars: pre-main sequence, stars: fundamental parameters

### 1. INTRODUCTION

The orbits of binary stars provide a way to measure the dynamical masses of the stellar components. Recent work on measuring the masses of pre-main sequence (PMS) stars has led to significant improvements in the evolutionary models computed at young stellar ages (e.g., Torres et al. 2013; Paxton et al. 2011; Baraffe et al. 2015; Feiden 2016; Simon et al. 2017). In this paper, we focus on measuring the visual orbits of 15 binary stars in the Ophiuchus star forming region that were initially resolved as binaries 10–20 yr ago (e.g., Ghez et al. 1993; Reipurth & Zinnecker 1993; Simon et al. 1995; Ageorges et al. 1997; Aspin et al. 1997; Koresko 2002; Barsony et al. 2003; Ratzka et al. 2005; Correia et al. 2006; McCabe et al. 2006). Several of these systems have not had measurements of their positions published since the time of their discovery. We also include two new detections of binaries in the Upper Centaurus-Lupus (UCL) cluster; these stars were initially included in a survey to detect tertiary companions in a sample of PMS spectroscopic binaries (Prato et al. in prep). If the distance is known, a visual binary orbit provides a measurement of the total system mass. At the distance of the Ophiuchus star forming region ( $\sim 130$  pc; Cheetham et al. 2015; Mamajek 2008; and references therein), binaries resolvable through adaptive optics (AO) imaging typically have periods on the order of decades (e.g., Schaefer et al. 2006, 2014). Therefore, the AO measurements presented here provide the groundwork for measuring high preci-

sion orbital parameters and dynamical masses in the future. In order to derive individual masses of the component stars, additional information is required, such as measurements of the astrometric motion of the components around their center of mass (Duchêne et al. 2006; Schaefer et al. 2012; Köhler et al. 2013, 2016) or the radial velocity variations in a double-lined spectroscopic binary (Boden et al. 2005; Torres et al. 2012; Simon et al. 2013; Le Bouquin et al. 2014).

In addition to providing dynamical masses as anchor points for the evolutionary tracks, the distribution of orbital parameters (eccentricities, semi-major axes) and mass ratios in binary systems provide clues to understanding the formation of binary stars (e.g., Duchêne & Kraus 2013; Reipurth et al. 2014). Moreover, about seven of the systems studied in this paper are part of triple or higher order multiple systems. The relative alignment of the orbits between the inner and outer pairs can probe the initial conditions of star formation (Fekel 1981; Sterzik & Tokovinin 2002; Reipurth et al. 2014; Tokovinin 2014). A similar assessment can be done by comparing the binary orbital plane with the orientation of circumstellar or circumbinary disks in the system (e.g., Kellogg et al. 2017). The frequency of coplanar or misaligned systems can provide insights into the formation of the multiple systems and their dynamical evolution over time.

Based on our AO observations and previous measurements available in the literature, we provide an overview on the status of the orbital motion and analysis for each

binary and triple system that was observed. We also indicate which systems show variability in their flux ratios.

## 2. ADAPTIVE OPTICS OBSERVATIONS

### 2.1. Target Selection

In the Ophiuchus star forming region, we selected previously known binary stars with separations in the range of 40–350 mas and  $R$ -band magnitudes within the sensitivity limits of the Keck AO system. The range of separations was selected so that the binaries could be resolved through AO imaging at Keck and would be expected to show a change in orbital motion since the time of their last observation. The observations presented in this paper do not represent a complete sample of binaries that meet these selection criteria.

Table 1 lists the binary stars that we observed, along with their right ascension, declination, distance, region, and spectral type. We assigned distances to each target based on their association with nearby star forming regions. Ortiz-León et al. (2017) measured the parallaxes for 12 stars in the Ophiuchus dark cloud Lynds 1688 and for three stars in the eastern streamer Lynds 1689. For our targets that are positionally coincident with Lynds 1688 and 1689, we quote the average distances measured by Ortiz-Leon et al. of  $137.3 \pm 1.2$  pc and  $147.3 \pm 3.4$  pc, respectively. One of our targets, ROXs 47A (DoAr 51) in Lynds 1689, has a direct parallax of  $143.2 \pm 1.0$  pc measured by Ortiz-Leon and we quote that value for the system. For Ophiuchus targets that lie in neither Lynds 1688 nor Lynds 1689, we use the distance of 130 pc adopted by Cheetham et al. (2015). For MML 50 and 53 we use the mean distance of  $140 \pm 2$  pc to UCL determined by de Zeeuw et al. (1999). Revised distances for each system will be available in the near future from the GAIA mission (Gaia Collaboration et al. 2016).

### 2.2. Keck NIRC2 Observations

We observed the sample of binary stars using the near-infrared camera NIRC2 (Wizinowich et al. 2000) on the 10-m Keck II Telescope at the W. M. Keck Observatory. We used the natural guide star AO system on all nights except for UT 2015 April 5 when we used the laser guide star. MML 50 and MML 53 were observed using natural guide star AO on all nights (including UT 2015 April 5). All images were taken with the narrow-field camera in NIRC2 which has a field of view of  $10''$ . Table 2 provides an observing log which lists the UT date and time of observation, target name, filter, AO rate, integration time per exposure, and number of images taken in each filter. Each image consisted of 10 coadded exposures. We obtained sets of 5–12 images dithered across the detector. We flatfielded the images using dark-subtracted dome flats and removed the sky background by subtracting

pairs of dithered images. Figure 1 shows example images of the multiples in our sample with the components identified.

We computed the separation, position angle, and flux ratio of the components in the multiple systems using point-spread function (PSF) fitting following the same methods described in Schaefer et al. (2014). For triple systems, we used the wide component as a simultaneous PSF to model the close pair. For wide binaries where the Airy rings of the PSF for each component did not overlap ( $\gtrsim 200$  mas), we used the primary component as the PSF to measure the relative separation of the secondary. Ordinarily, for close binaries with overlapping PSFs and no wide component in the field of view, we typically use a separate observation of a single star PSF reference observed either immediately before or after the target using the same AO frame rate. However, because the targets are at southern declinations and were observed at moderate airmasses ( $z = 1.4$ – $2.0$ ), the AO correction between nearby targets was not always stable, leading to mis-matched PSF shapes. The variability in the shape of the central core and structure in the Airy ring of the PSF can be seen by comparing images of different binaries observed on the same night in Figure 1. To overcome this difficulty, we created an “effective PSF” (ePSF) directly from the blended binary components.

To create the ePSF, we cross-correlated the central cores of the PSFs from each component to align the images, scaled the fluxes to match their brightnesses, and rejected pixels with the highest counts from the averaged PSF. This process eliminates the blended side of the PSF from each component, providing the PSF of an effectively “single” star as shown in Figure 2. In each case where we used an ePSF (indicated in the last column of Table 2), we compared the positions with those computed from using a separate observation of a single PSF star. In all cases, the  $\chi^2$  between the data and binary model were lower when using the ePSF. For binaries with separations  $\lesssim 70$  mas (i.e., MML 53 and VSSG 14), the cores of the components overlapped too much, so we could not create a suitable ePSF and had to use a separate observation of a single star as the PSF. We tested the reliability of creating an ePSF using the triple star EM\* SR 24. For this system, we used SR 24S as a simultaneous PSF to model the  $\sim 100$  mas close pair SR 24 Na,Nb. We also created an ePSF directly from the components in the close pair. The positions derived for the close pair were consistent within 0.90 mas on UT 2014 July 06 and 0.39 mas on UT 2015 July 22, both within the  $1\sigma$  uncertainties of the two methods.

We corrected the binary positions using the geometric distortion solutions published by Yelda et al. (2010) prior to the optical realignment of the AO system on 2015 April 13 and by Service et al. (2016) after the re-

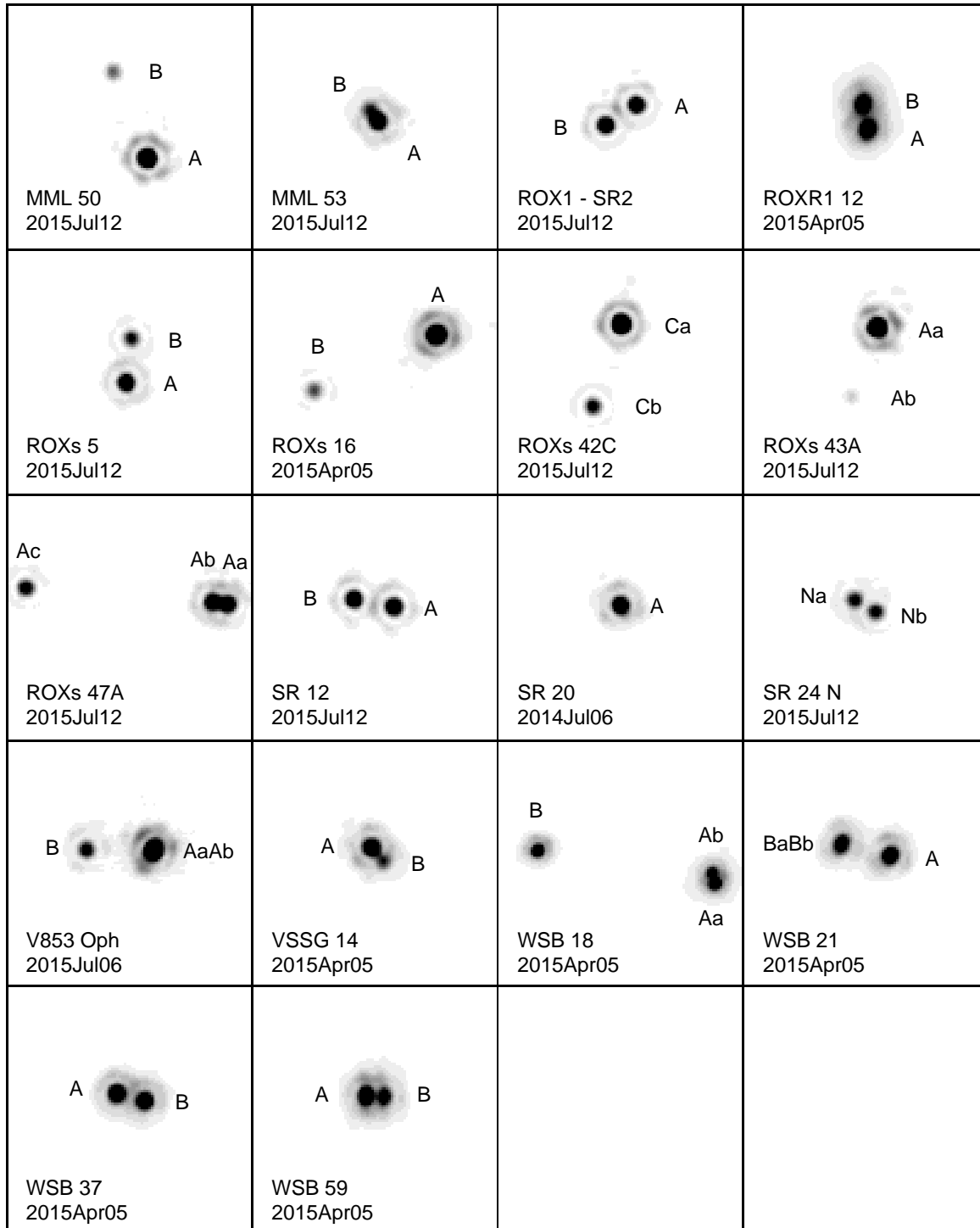


**Figure 1.** Keck NIRC2 AO images of PMS multiple systems in the Ophiuchus and UCL star forming regions. Each panel is  $\sim 1''$  wide, except for the WSB 18 panel which is  $\sim 1.5''$  wide. North is up and east is to the left. Wide companions with separations larger than  $1''$  are not shown. For systems where the components are nearly equal brightness, the identification of the A and B components might vary in the literature. In most panels, the flux scale saturates at 0.4 times the maximum value, except for MML 50, ROXs 16, ROXs 42C, ROXs 43A, and V853 Oph which saturate at 0.2 times the maximum to bring out the faint companions.

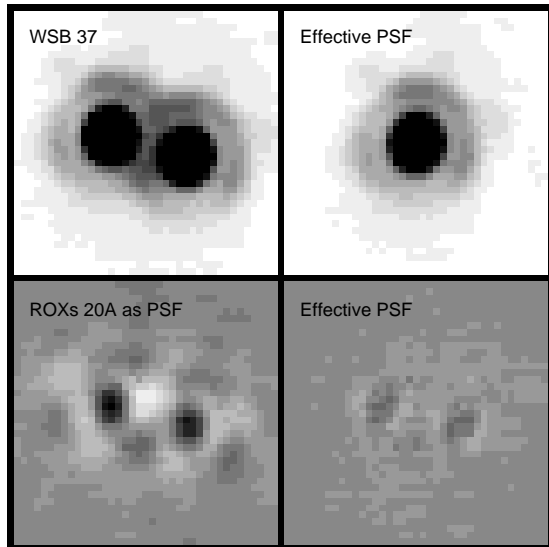


**Figure 2.** Top left: Image of the binary WSB 37 on UT 2015 Apr 5. The binary is separated by 117 mas. Top right: Effective PSF created by aligning and coadding the PSFs from the two components after rejecting pixels with the highest number of counts. Bottom: Residuals between WSB 37 and the model binary created using a separate image of ROXs 20A as the PSF (left) and using the effective PSF (right). The two residual panels are plotted on the same scale, showing the improvement in the binary fit when using the effective PSF.

alignment. For the earlier AO observations, we used a plate scale of  $9.952 \pm 0.001$  mas pixel $^{-1}$  and subtracted  $0^{\circ}252 \pm 0^{\circ}009$  from the raw position angles to correct for the orientation of the camera relative to true north. After 2015 April 13, we used a plate scale of  $9.971 \pm 0.004$  mas pixel $^{-1}$  and subtracted  $0^{\circ}262 \pm 0^{\circ}020$  from the measured position angles. Table 3 presents the Julian year, binary separation, position angle measured east of north, and flux ratios measured in each filter. The positions were averaged over the measurements from individual frames in the  $H$  and  $K$  bands, and uncertainties were computed from the standard deviation. These filters provide a good compromise between angular resolution and PSF stability. For systems with more than two components, we list the measurements for each pair of stars separately. In Figure 3 we show how the  $K$ -band flux ratios change over time.

### 3. ANALYSIS OF ORBITAL MOTION

We combined our AO measurements of the binary positions with previously published values from the literature. In several cases we found no published reports of additional measurements of the binary separations since the time of their discovery over 10–20 yr ago. With such limited orbital coverage, it was not possible to compute orbital solutions. For binaries with enough measurements to begin mapping the curvature of the orbit, we assessed the range of possible orbital solutions

using the statistical approach outlined by Schaefer et al. (2006, 2014). In general, we searched for possible orbital solutions out to periods of 500 years, eccentricities from 0 to 0.99, and times of periastron passage that covered the full range of the orbital periods. In three cases where the binaries have sufficient orbital coverage (ROXs 47A, EM\* SR 20, and EM\* SR 24), we computed preliminary values for the orbital period ( $P$ ), time of periastron passage ( $T$ ), eccentricity ( $e$ ), angular semi-major axis ( $a$ ), inclination ( $i$ ), position angle of the line of nodes ( $\Omega$ ), and the angle between the node and periastron ( $\omega$ ). We discuss the results for each system in more detail below.

#### 3.1. MML 50

MML 50 is a young star in the UCL cluster (Wichmann et al. 1997; Mamajek et al. 2002). It was selected as a PSF star for MML 53, but was discovered to be binary with a separation of 376 mas with a flux ratio of 0.10 in the near infrared. The system could be a triple because White et al. (2007) identified the brighter component as a double-lined spectroscopic binary based on the presence of doubled lines.

#### 3.2. MML 53

MML 53 is an X-ray active, lithium rich star in the UCL cluster (Wichmann et al. 1997; Mamajek et al. 2002). It was identified as a double-lined spectroscopic binary by White et al. (2007) based on the doubling of photospheric spectral lines observed in the visual. The system was later discovered to be an eclipsing binary with a period of 2.1 days (Hebb et al. 2010). Subsequently, a double-lined spectroscopic orbit was determined (Hebb et al. 2011). A tertiary companion was detected on the basis of its spectral signature and a change in the systematic velocity of the eclipsing binary (Hebb et al. 2010, 2011).

We resolved the tertiary companion at a separation of 57 mas using Keck NIRC2 AO on UT 2014 July 5. We resolved this companion again on two nights in 2015. Based on the effective temperatures of the three components derived by Hebb et al. (2010) and the near-infrared flux ratio of  $\sim 0.4$  for the spatially resolved pair, we expect that the eclipsing binary is the brighter component in our NIRC2 observations. The tertiary companion shows significant orbital motion over two years, as shown in Figure 4. However, we have not yet mapped enough of the orbit to place meaningful constraints on the orbital parameters.

#### 3.3. ROX 1

ROX 1 (EM\* SR 2) was first detected as a binary through micrometer observations by Heintz (1980). The binary was subsequently resolved through speckle imaging (Ghez et al. 1993, 1995; Ratzka et al.

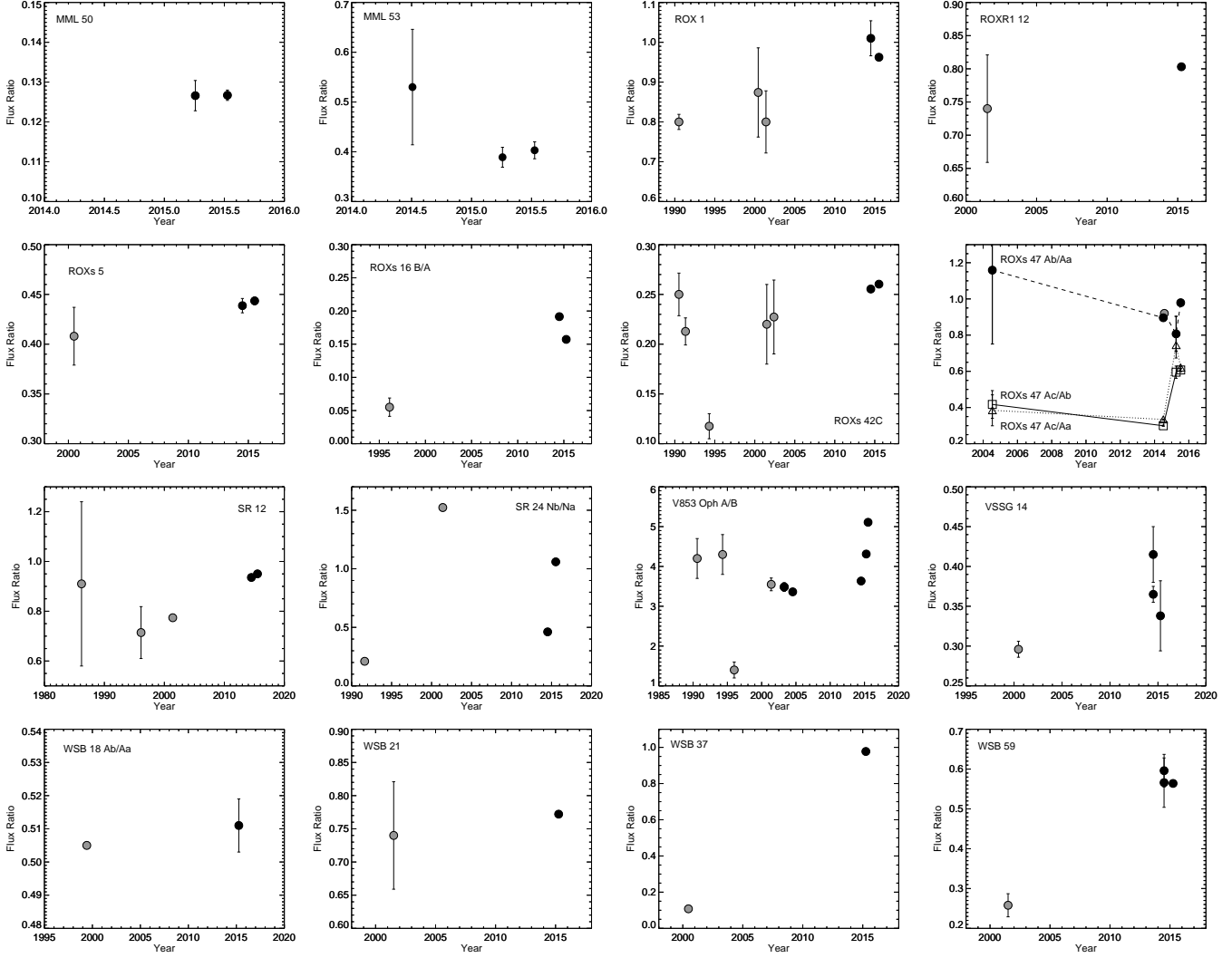


**Figure 3.**  $K$ -band flux ratios for each system as a function of time. The black circles show our AO measurements while the gray circles show previously published measurements from the literature (see references in notes on individual systems in Section 3).

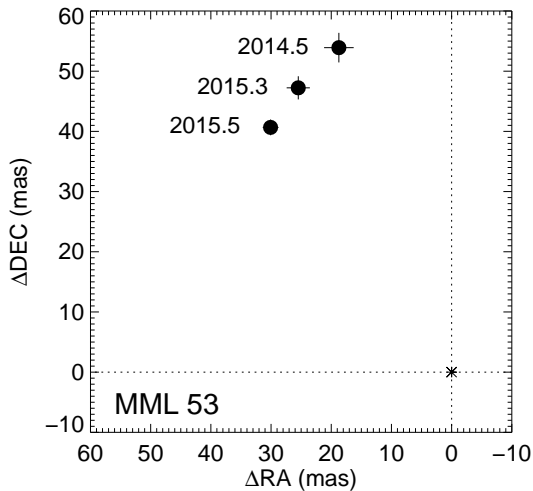


**Figure 4.** Orbital motion measured for MML 53 based on our Keck NIRC2 observations.

2005; McCabe et al. 2006) and shift-and-add techniques (Aspin et al. 1997). We resolved the system twice in 2014–2015 using AO imaging. Figure 5 shows that there is a surprising amount of scatter in the measured orbital motion and that determining a well-defined orbital period is not yet possible. Given that the components are nearly equal brightness, we flipped some of the position angles by  $180^\circ$  to find a realistic set of orbital positions. It is possible that our identification of the two components at each epoch is not correct; additional measurements in the future to further map the orbital motion should help resolve these possible discrepancies.

A statistical analysis of orbital solutions that fit the existing data indicates that the orbital period is greater than 60 yr, with the  $1\sigma$  confidence interval extending out to the search range of 500 yrs. In Figure 5 we plot examples of three orbits that fit the data. These orbits were selected to produce a total mass of  $\sim 1.9M_\odot$  at

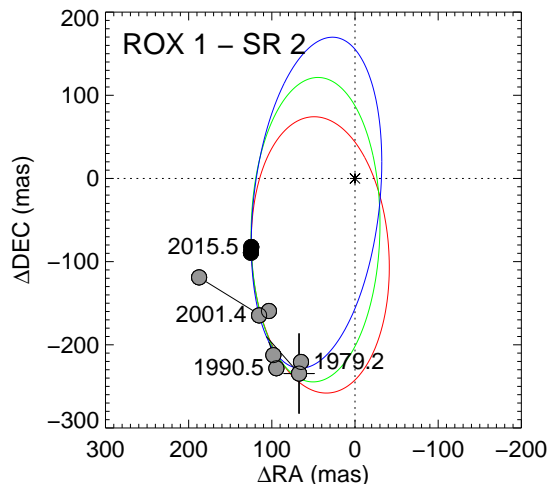


**Figure 5.** Orbital motion measured for ROX 1 (EM\* SR 2) based on our AO observations (black circles) and published values from the literature (gray circles; Heintz 1980; Ghez et al. 1993, 1995; Aspin et al. 1997; Ratzka et al. 2005; McCabe et al. 2006). Overplotted are three sample orbits with periods ranging from 110–130 yr and total masses of  $\sim 1.9M_{\odot}$  for a distance of 130 pc.

a distance of 130 pc. The approximate total mass was estimated by assuming two equal mass components, each with a spectral type of G9 (Torres et al. 2006) and using the effective temperature and mass estimates computed by Kraus & Hillenbrand (2007). Without the constraint on the total mass, the orbit fits tend to prefer highly eccentric, high mass orbits.

### 3.4. ROXR1 12

ROXR1 12 was resolved as a binary through speckle observations by Ratzka et al. (2005) in 2001. We resolved the system again using AO imaging in 2015. Figure 6 shows significant orbital motion between the two epochs, although with only two measurements, the coverage is not sufficient for fitting a binary orbit yet.

### 3.5. ROXs 5

ROXs 5 was resolved as a binary through speckle observations by Ageorges et al. (1997) and Ratzka et al. (2005). We resolved the system two times using adaptive optics imaging at Keck. Figure 7 shows the orbital motion of ROXs 5. The position angle of the speckle measurement by Ageorges et al. (1997) in 1994.3 has been flipped by  $180^{\circ}$ . At the published position angle of  $130^{\circ}$ , a very eccentric family of orbits fit the data with a minimum total mass of  $12.6 M_{\odot}$  assuming a distance of 130 pc, inconsistent with the K7 spectral type of the system (Bouvier & Appenzeller 1992). After flipping the position angle of the discovery measurement, a statistical analysis of orbital solutions that fit the data indicates that the orbital period is greater than 36 yr, with the  $1\sigma$

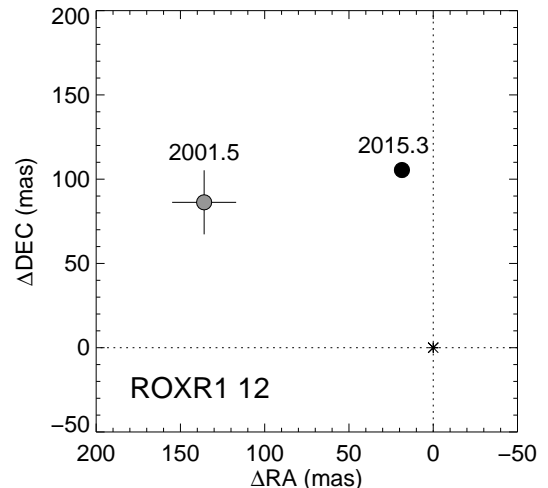


**Figure 6.** Orbital motion measured for ROXR1 12 based on our AO observations (black circle) and the speckle measurement from Ratzka et al. (gray circle; 2005).

confidence interval extending out to the search range of 500 yr. These orbital solutions provide a more realistic minimum mass of  $\sim 0.87 M_{\odot}$ .

In Figure 7 we show examples of three orbits that fit the data. When selecting the orbits to plot, we placed an upper limit of  $\sim 1.2 M_{\odot}$  on the total system mass, determined by assuming two equal mass components, each with a spectral type of K7 (Bouvier & Appenzeller 1992), and using the table of effective temperatures and masses computed by Kraus & Hillenbrand (2007). This removed highly eccentric, high mass orbits from the range of possible solutions.

### 3.6. ROXs 16

ROXs 16 A,B was resolved as a binary with a separation of  $\sim 590$  mas through speckle and shift-and-add techniques (Ageorges et al. 1997; Costa et al. 2000; Ratzka et al. 2005). A possible close companion (ROXs 16 Aa,Ab) was detected during the speckle observations by Ratzka et al. (2005), although the authors caution that the “probable third component of ROXs 16 is too close to distinguish between an elongated structure and a point source”. Fitting the individual Keck AO images as a triple system resulted in possible separations for the close pair ranging between 10–20 mas over a wide range of position angles. Given the large range of positions below the limit of what we can reliably measure using a simultaneous PSF at Keck (e.g., Schaefer et al. 2012), we do not consider the detection reliable. Figure 8 shows the orbital motion observed in the wide A,B pair. A statistical analysis of the orbital motion indicates that the orbital period is greater than 42 yr, with the  $1\sigma$  confidence interval extending out to the search range of 500 yr. As shown in Figure 3, the *K*-band flux ratio of

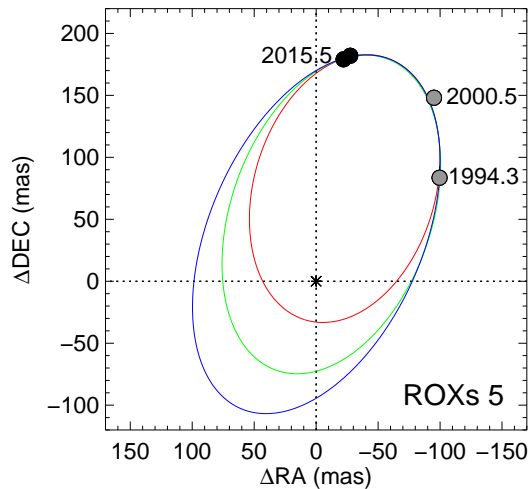


**Figure 7.** Orbital motion measured for ROXs 5 based on our AO observations (black circles) and published measurements from the literature (gray circles; [Ageorges et al. 1997](#); [Ratzka et al. 2005](#)). We flipped the position angle of the speckle measurement by [Ageorges et al. \(1997\)](#) in 1994.3 by  $180^\circ$ . Overplotted are three sample orbits with periods ranging from 51–84 yr and total masses of  $0.9 - 1.2M_\odot$  for a distance of 130 pc.

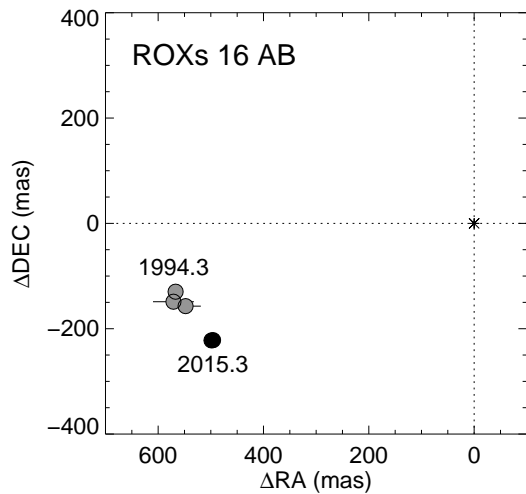


**Figure 8.** Left: Orbital motion measured for ROXs 16 A,B based on our AO observations (black circles) and previously published measurements in the literature (gray circles; [Ageorges et al. 1997](#); [Costa et al. 2000](#); [Ratzka et al. 2005](#)).

ROXs 16 B relative to A has changed significantly over time.

### 3.7. ROXs 42C

ROXs 42C (NTTS 162814-2427) was identified as a double-lined spectroscopic binary with a period of 36 days by [Mathieu et al. \(1989\)](#). It was discovered to have a wide tertiary component with a separation of

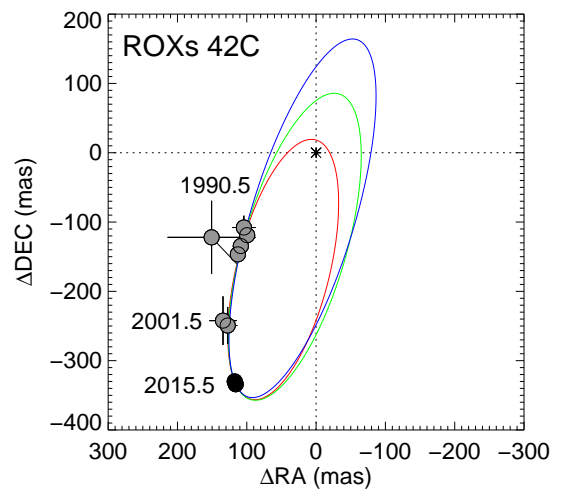
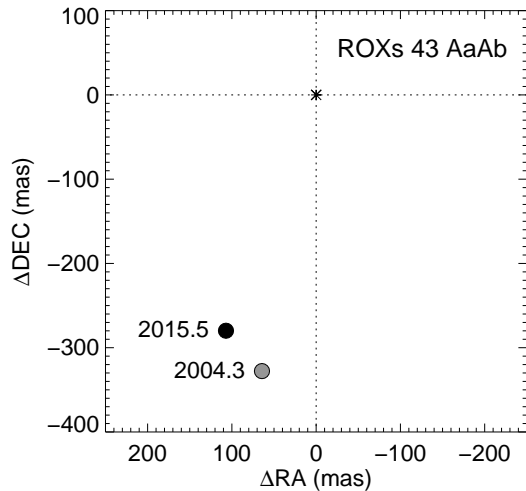


**Figure 9.** Orbital motion measured for ROXs 42C based on our AO observations (black circles) and published measurements in the literature (gray circles; [Ghez et al. 1993, 1995](#); [Aspin et al. 1997](#); [Barsony et al. 2003](#); [Ratzka et al. 2005](#)). Overplotted are examples of orbital solutions with periods ranging from 80 to 120 yr.

150 mas through speckle interferometry ([Ghez et al. 1993](#)). The orbital motion of the visual pair has been monitored through speckle imaging and shift-and-add techniques ([Ghez et al. 1993, 1995](#); [Aspin et al. 1997](#); [Barsony et al. 2003](#); [Ratzka et al. 2005](#)). We resolved the system during two AO observations. Figure 9 shows the orbital motion for ROXs 42C. A statistical analysis of orbital solutions that fit the data indicates that the orbital period is greater than 56 yr, with the  $1\sigma$  confidence interval extending out to the search range of 500 yr.

### 3.8. ROXs 43 Aa,Ab,B

ROXs 43 A and B are a  $\sim 4''.5$  visual pair ([Barton 1951](#); [Bouvier & Appenzeller 1992](#); [Reipurth & Zinnecker 1993](#); [Simon et al. 1995](#); [Ageorges et al. 1997](#); [Ratzka et al. 2005](#); [Correia et al. 2006](#); [McCabe et al. 2006](#)). ROXs 43A was detected as a single-lined spectroscopic binary with a period of 89 days ([Mathieu et al. 1989](#)). The spectroscopic binary was discovered to have an additional companion with a separation of 334 mas and a flux ratio of 0.05 through adaptive optics observations by [Correia et al. \(2006\)](#). This companion was not detected in the speckle observations by [Ghez et al. \(1993\)](#) or [Ratzka et al. \(2005\)](#). ROXs 43B was discovered to have a close companion with a projected separation of 16 mas through the lunar occultation observations by [Simon et al. \(1995\)](#). Therefore, the system is a quintuple. During our AO observations at Keck in 2015, we resolved the 300 mas pair ROXs 43 Aa,Ab; the orbital motion is shown in



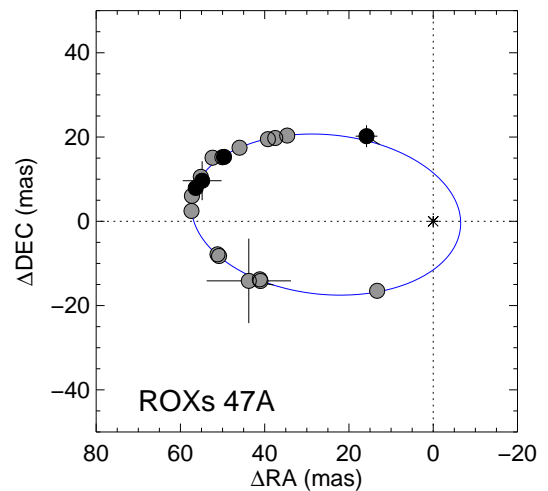
**Figure 10.** Orbital motion measured for ROXs 43 Aa,Ab based on our AO observation (black circle) and the AO observation by Correia et al. (gray circle; 2006).

Figure 10. We attempted to fit ROXs 43 Ba,Bb as a close binary using ROXs 43 Aa as the PSF, but could not derive a reliable separation ( $\rho < 20$  mas).

### 3.9. ROXs 47A

ROXs 47A (DoAr 51) was resolved as a triple system by Barsony et al. (2003). The wide pair has a separation of  $\sim 790$  mas (Barsony et al. 2003; Ratzka et al. 2005; McCabe et al. 2006). The orbital motion of the close pair has been resolved through speckle interferometry, aperture masking, and VLBA radio observations (Barsony et al. 2003; Cheetham et al. 2015; Rizzuto et al. 2016; Ortiz-León et al. 2017). An orbit for the close pair with a period of 8.2 yr and a semi-major axis of 33 mas was computed by Rizzuto et al. (2016). Based on VLBA radio observations, Ortiz-León et al. (2017) revised the relative orbit and computed the astrometric center of mass motion and a geometric parallax of  $6.983 \pm 0.050$  mas ( $143.2 \pm 1.0$  pc). This astrometric solution provided individual masses of  $0.791 \pm 0.014 M_{\odot}$  and  $0.781 \pm 0.042 M_{\odot}$  for the components in the close pair.

We resolved the triple system on four nights between 2004–2015 using adaptive optics imaging at Keck. Figure 11 shows the orbital motion of the close pair. Our AO observations are consistent with the previously published measurements. An orbit fit to all of the available data yields the orbital parameters in Table 4 which are consistent with those published by Rizzuto et al. (2016) and Ortiz-León et al. (2017). The astrometric motion of the close pair relative to the wide component based on our AO observations is too sparse to model the center of mass motion, however, the motion is consistent with the astrometric orbit published by Ortiz-León et al. (2017).



**Figure 11.** Orbital motion measured for ROXs 47 Aa,Ab (DoAr 51) based on our AO observations (black circles) and previously published measurements (gray circles; Barsony et al. 2003; Cheetham et al. 2015; Rizzuto et al. 2016; Ortiz-León et al. 2017). Overplotted is the best fitting visual orbit with a period of 8.1 yr.

As shown in Figure 3, the  $K$ -band flux ratio of ROXs 47 Ac relative to Aa and Ab varied by a factor of  $\sim 2$  in 2014–2015, while the flux ratio of Ab relative to Aa has changed by only factor of  $\sim 1.2$ . This suggests that Ac is likely the most variable component.

### 3.10. EM\* SR 12

SR 12 (HBC 263) was first detected as a binary during a lunar occultation (Simon et al. 1987). The orbital motion of the binary has been mapped through lunar occultations, speckle interferometry, and imaging (Simon et al. 1987; Zinnecker & Perrier 1988; Simon et al. 1995; Costa et al. 2000; Allen et al. 2002; McCabe et al. 2006). The system also has a faint, substellar companion (SR 12 C) at a separation of  $8''.8$  (Allen et al. 2002; Kuzuhara et al. 2011; Bowler et al. 2014). SR 12 C was outside of the field of view of the NIRC2 images. Figure 12 show the orbital motion measured for SR 12 B relative to A. Fitting an orbit to the data provides an improved  $\chi^2$  compared with linear motion, but the coverage is so limited that we cannot place strong constraints on the orbital parameters. A statistical analysis of orbits that fit the data indicates that the orbital period must be greater than 62 yr with the  $1\sigma$  confidence interval extending out to the search range of 500 yr. The  $K$ -band flux ratio of SR 12 has increased by a factor of  $\sim 1.3$  since the previous measurements in 1996–2001.

### 3.11. EM\* SR 20

SR 20 (HBC 643) was first detected as a binary with a separation of 71 mas by Ghez et al. (1993).



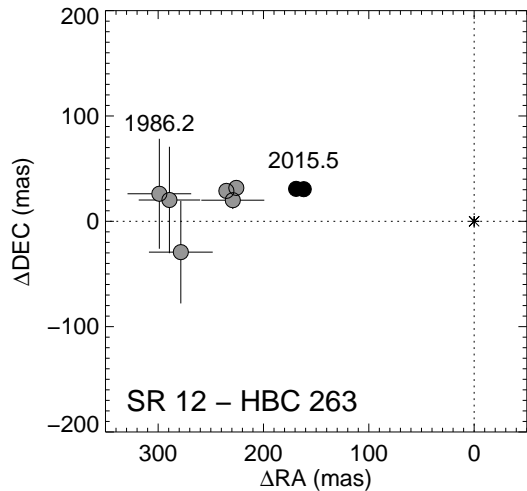


**Figure 12.** Orbital motion measured for EM\* SR 12 A,B based on our AO observations (black circles) and previously published measurements (gray circles; [Simon et al. 1987](#); [Zinnecker & Perrier 1988](#); [Simon et al. 1995](#); [Costa et al. 2000](#); [Allen et al. 2002](#); [McCabe et al. 2006](#)).

The orbital motion has been mapped through speckle imaging and aperture masking ([Ghez et al. 1993, 1995](#); [Cheetham et al. 2015](#)). The system was unresolved on three occasions reported by [Richichi et al. \(1994\)](#) and [Ghez et al. \(1995\)](#). We observed the system using AO imaging on UT 2014 July 6; the data suggest that the image is not a single star, but without a simultaneous PSF in the field of view we could not measure a reliable binary separation. The separation measured from individual frames varied between 20–54 mas over a wide range of position angles. Likewise, we were not able to measure a reliable separation during aperture masking observations that we obtained on UT 2015 July 12. As shown in Figure 13, the published measurements span nearly one full orbital period ( $P \sim 23.2$  yr). We fit an orbit to these data and obtained the preliminary orbital parameters in Table 4. However, because the observations all lie on the same side of the orbit and there is a large deviation in the position of the discovery observation, most of the orbital parameters have large uncertainties. The uncertainties were estimated by exploring the  $1\sigma$  confidence intervals using the grid search procedure described in [Schaefer et al. \(2006\)](#). At an assumed distance of 130 pc, a statistical analysis of the orbits that fit the data indicate a median total mass of  $0.7^{+1.2}_{-0.3} M_{\odot}$ .

### 3.12. EM\* SR 24N

SR 24 S and N are separated by  $6''$  ([Struve & Rudkjøbing 1949](#); [Ratzka et al. 2005](#); [McCabe et al. 2006](#); [Correia et al. 2006](#)). Our AO observations indicate that the relative separation has

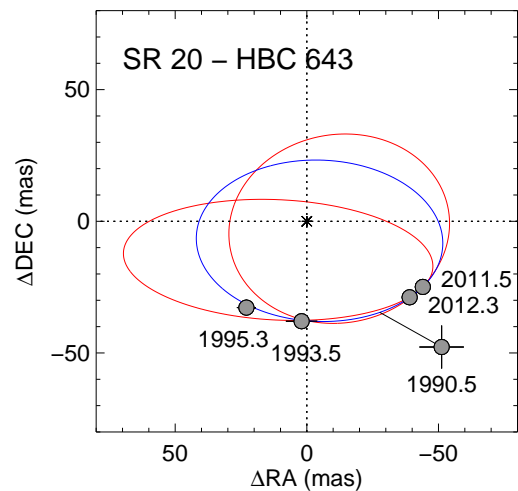


**Figure 13.** Orbital motion measured for SR 20 (HBC 643) as measured by [Ghez et al. \(1993, 1995\)](#) and [Cheetham et al. \(2015\)](#). The blue line shows the best fit orbit with a period of 23.3 yr while the red lines shows orbits within the  $1\sigma$  confidence interval in the inclination.

remained constant over the past two decades. SR 24 N (WSB 41) is a close binary with a separation of  $\sim 100$  mas ([Simon et al. 1995](#); [Costa et al. 2000](#); [Correia et al. 2006](#); [McCabe et al. 2006](#)). [Cheetham et al. \(2015\)](#) did not resolve the close pair during their aperture masking observations. We resolved all three components in the SR 24 system during two AO imaging observations in 2014–2015. Figure 14 shows the orbital motion observed for the close binary SR 24 N. A statistical analysis of orbital solutions that fit the data indicates that the  $1\sigma$  confidence interval on the orbital period extends from 78 to 216 yr. The preliminary ranges for each of the orbital parameters are listed in Table 4. Sufficient curvature has been mapped to provide well-defined  $1\sigma$  bounds on the total mass. Assuming that the system is located in Lynds 1688 at a distance of 137.3 pc, the total mass of SR 24N is  $1.24 \pm 0.24 M_{\odot}$ .

The relative brightness of the two components in SR 24N has varied significantly, with the  $K$ -band flux ratios (Nb/Na) varying between 0.46 to 1.5, as shown in Figure 3. There are disks around both SR 24S (e.g., [Pinilla et al. 2017](#)) and SR 24N ([Greene et al. 1994](#); [Martin et al. 1998](#)). Recent ALMA observations indicate that the disks are misaligned ([Fernández-López et al. 2017](#)). The continuum emission detected around SR 24N is unresolved by the ALMA observations at a resolution of 150 mas. Based on the  $1\sigma$  confidence intervals from the orbital fitting, the minimum and maximum projected separations between Na and Nb range between 42–47 mas and 175–370 mas, suggesting that the continuum emission is likely from a circumstellar disk around one of the northern components.

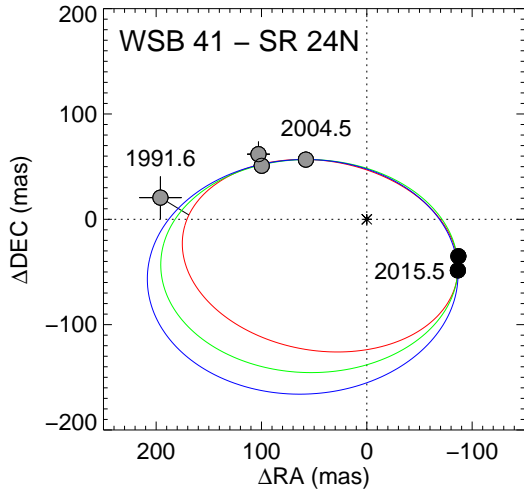


**Figure 14.** Orbital motion measured for SR 24 Na,Nb based on our AO observations (black circles) and previously published measurements (gray circles; [Simon et al. 1995](#); [Correia et al. 2006](#); [McCabe et al. 2006](#)). Overplotted are three examples of orbits that fit the data with orbital periods of 80–110 yr.

The semi-major axis of 600 mas for the CO line emission detected by ALMA is larger than the dimensions of the binary orbit, suggesting that it is likely from a circumbinary disk. This geometry is similar to the interpretation by [Andrews & Williams \(2005\)](#). The size and orientation of the circumbinary disk and the binary orbit on the plane of the sky are shown in Figure 15. Comparing the preliminary visual orbital parameters for the close binary with the orientation of the disk around SR 24N indicates a relative of alignment (e.g., [Fekel 1981](#); [Kellogg et al. 2017](#)) of  $37^{+19}_{-9}$  or  $96^{+17}_{-21}$  between the binary orbit and the disk (the two possibilities are a result of the  $180^\circ$  ambiguity in  $\Omega$  for the visual orbit). Obscuration by the disk around SR 24N could be causing the observed photometric variability; monitoring the flux ratio in the  $K$  and  $L$  bands could help identify the source of the variability ([Prato & Simon 1997](#); [Beck et al. 2004](#)).

### 3.13. V853 Oph

The orbital motion of the wide pair V853 Oph A,B with a separation of  $\sim 300$  mas has been monitored using speckle interferometry, lunar occultation, shift-and-add techniques, the Fine Guidance Sensors onboard the *Hubble Space Telescope*, and adaptive optics imaging ([Ghez et al. 1993](#); [Simon et al. 1995](#); [Aspin et al. 1997](#); [Costa et al. 2000](#); [McCabe et al. 2006](#); [Schaefer et al. 2006](#)). [Simon et al. \(1995\)](#) discovered a close companion to the primary (Aa,Ab) during a lunar occultation observation. We obtained three additional observations of the system using AO imaging at Keck in 2014–2015. On UT 2014 Jul 6, there were significant residuals in

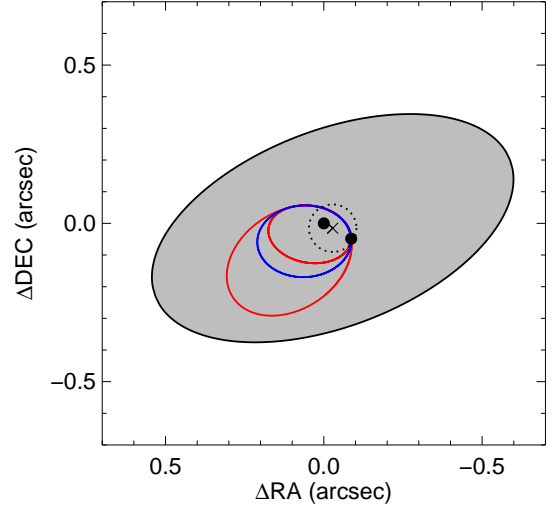


**Figure 15.** Relative orientation of the SR 24 Na,Nb binary orbit compared with the circumbinary disk. The filled circles show the relative separation of Na and Nb in 2015.5; the position of Na is fixed at the origin. The blue line shows the best fit binary orbit with a period of 111 yr while the red lines show the smallest and largest orbits in the  $1\sigma$  confidence interval. The cross marks the relative offset of the continuum emission detected by [Fernández-López et al. \(2017\)](#) in 2015 compared with the infrared positions of Na and Nb relative to SR 24S. The small dotted circle represents the ALMA resolution limit of  $0.15''$  during the continuum observations. The shaded ellipse shows the orientation and size of the CO disk in the plane of the sky.

the PSF fitting when modeling V853 Oph A as a single source, indicating that the PSF of V853 Oph A is elongated in comparison to B. For these data, we modeled V853 Oph Aa,Ab as a close binary using V853 Oph B as the PSF and obtained a consistent separation of  $23.51 \pm 0.97$  mas. The difference in Akaike’s information criterion ([Burnham & Anderson 2002](#)) between the binary and triple fits ranged between 520–1000 for the individual images, indicating a significant improvement in the  $\chi^2$ . For our data from the two nights in 2015, we attempted to fit the system as a triple, but the range of separations derived from the individual images varied by a factor of two (14–27 mas on 2015 April 5 and 9–17 mas on 2015 July 12). The difference in Akaike’s information criterion on these nights was significant (82–302), indicating an elongation compared with a point source, however the separation and position angle could not be measured reliably.

In Table 3 we present the wide pair (V853 Oph B,A) separations for all nights, and the possible detection of the close companion in 2014. We also present two updated positions of the wide pair from [Schaefer et al. \(2006\)](#) that have been corrected for geometric distortions. Figure 16 shows the orbital motion of V853 Oph A relative to the fainter wide component B. A statistical analysis of possible orbits that fit the data indicates that

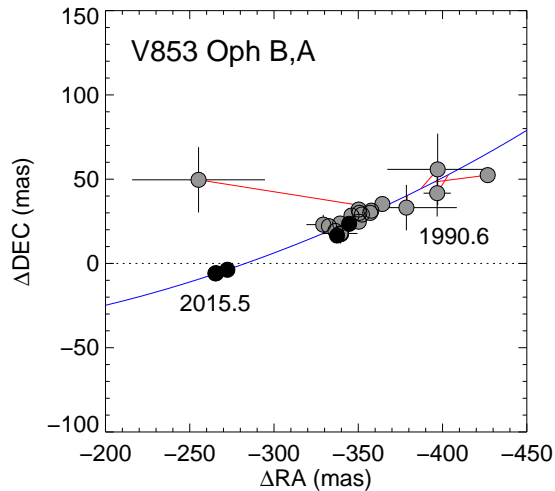


**Figure 16.** Orbital motion measured for V853 Oph A relative to the fainter wide component B based on our AO observations (black circles) and previously published measurements (gray circles; Ghez et al. 1993; Simon et al. 1995; Aspin et al. 1997; Costa et al. 2000; McCabe et al. 2006; Schaefer et al. 2006). Overplotted in blue is a sample orbit with a period of 400 yr. The red line segments connect the measurements with the predicted positions along the orbit. The measured separation of the most discrepant point was near the resolution limit of the telescope in the observed *N*-band (McCabe et al. 2006).

the period is longer than 80 yr, with the  $1\sigma$  confidence interval extending out to the search range of 500 yr. As shown in Figure 3, the *K*-band flux ratio of V853Oph A relative to B has varied significantly. Schaefer et al. (2006) showed that most of the *V*-band variability is associated with the primary V853 Oph A. Both wide components are classified as classical T Tauri stars with disks (Geoffroy & Monin 2001).

### 3.14. VSSG 14

The close companion to VSSG 14 was discovered through a lunar occultation with a projected separation of 101 mas (Richichi et al. 1994). It was resolved through speckle imaging eight years later (Ratzka et al. 2005). We resolved the close companion during three AO observations in 2014–2015. Figure 17 shows the current orbital motion observed for VSSG 14. A statistical analysis of orbital solutions that fit the existing data indicates that the orbital period is greater than 8.7 yr, with the  $1\sigma$  confidence interval extending out to the search range of 500 yrs. There is not yet enough curvature to place reasonable estimates on the total mass.

### 3.15. WSB 18

WSB 18 is a triple system. The wide pair is separated by  $1.0''$  (Reipurth & Zinnecker 1993; Koresko 2002; Ratzka et al. 2005; McCabe et al. 2006). A close

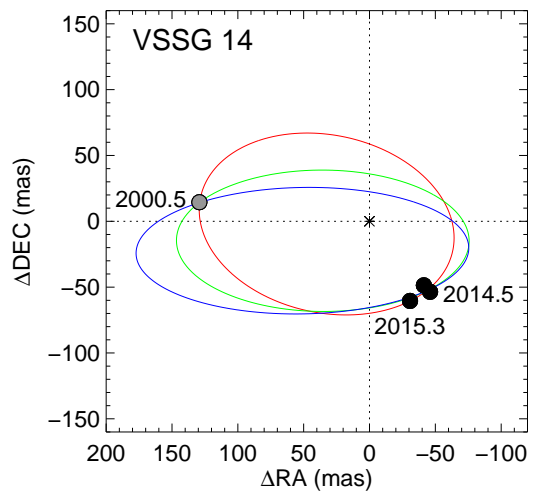


**Figure 17.** Orbital motion measured for VSSG 14 based on our AO observations (black circles) and the speckle measurement (gray circle) from Ratzka et al. (2005). Overplotted are examples of orbital solutions with periods ranging from 25–50 yr.

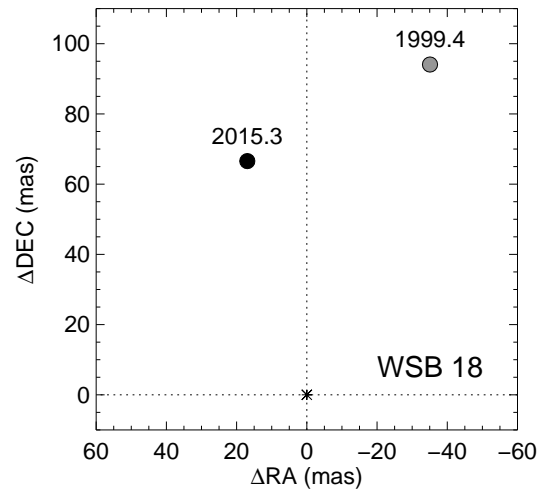


**Figure 18.** Orbital motion measured for the close pair in WSB 18 based on our AO observation (black circle) and the speckle measurement (gray circle) from Koresko (2002).

companion with a separation of 100 mas was discovered by Koresko (2002) during speckle observations. We resolved all three components in the triple system during our AO observation in 2015. Figure 18 shows the orbital motion observed for the close pair. The companion has moved significantly since its detection in 1999.

### 3.16. WSB 21

WSB 21 was discovered to be a binary with a separation of 121 mas through speckle observations by Ratzka et al. (2005). We resolved the companion dur-

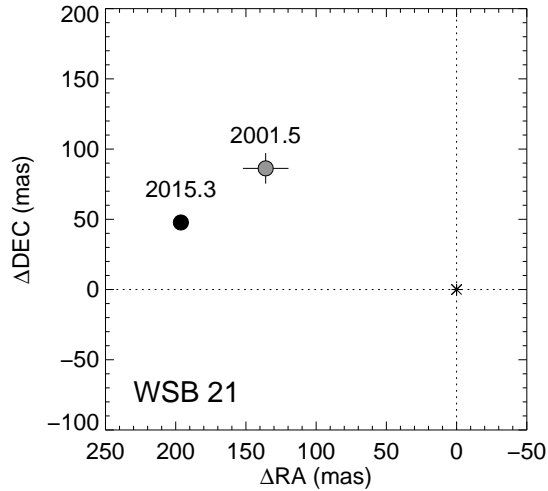


**Figure 19.** Orbital motion measured for WSB 21 based on our AO observations (black circle) and the speckle measurement (gray circle) from Ratzka et al. (2005).

ing our AO observations in 2015. Figure 19 shows the orbital motion. The PSF fitting of the AO data using the primary as the PSF showed strong residuals in the secondary, indicating that the PSF of the secondary is more elongated than the primary. We attempted to fit the system as a triple and found a consistent solution across all images and filters by fitting the secondary as a close binary with a separation of only 21 mas. This possible detection of WSB 21 as a triple must be confirmed in future observations. We list the separation and position angle for both the binary and triple solutions in Table 3. Figure 20 shows a comparison of the binary and triple fits. The separation of the A and B components are close enough on the detector ( $\sim 200$  mas) that we do not expect geometric distortion to be the cause of the difference in the PSF shapes.

### 3.17. WSB 37

WSB 37 was resolved as a binary with a separation of 161 mas through speckle observations by Ratzka et al. (2005). We resolved the system during our AO observations in 2015. There is a  $180^\circ$  ambiguity in the position angle of the original speckle observation. The direction of motion could be clarified with additional measurements along the orbit. Figure 21 shows two possibilities for how much the binary has moved over fifteen years since its discovery. The option at a position angle of  $245^\circ$  is more consistent in a dynamical sense with a pair of low-mass stars. The  $K$ -band flux ratio of WSB 37 has increased by nearly a factor of 10 compared with the initial measurement by Ratzka et al. (2005).

### 3.18. WSB 59

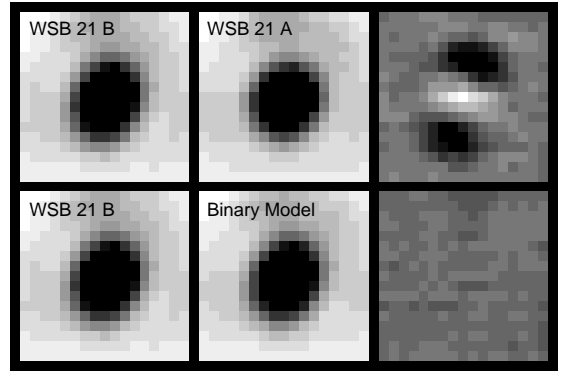


**Figure 20.** Comparison of binary and triple fits for WSB 21. The top row shows the fainter component (WSB 21 B), the brighter component (WSB 21 A) scaled to the brightness of WSB 21 B, and the residuals between the images. The residuals show that WSB 21 B is elongated in comparison to A. The bottom row shows WSB 21 B, a binary model using WSB 21 A as a simultaneous PSF, and the residuals between the images showing an improved fit. In both rows, the scale of the residual plots was shifted and expanded by a factor of four to bring out the finer details.

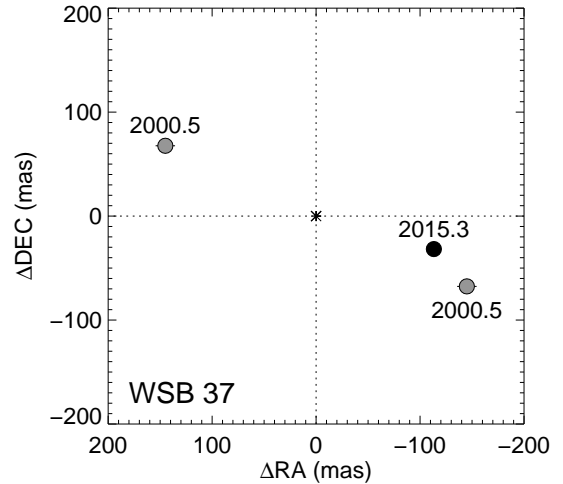


**Figure 21.** Orbital motion measured for the close pair in WSB 37 based on our AO observations (black circle) and the speckle measurement (gray circle) from Ratzka et al. (2005). There is a  $180^\circ$  ambiguity in the position angle of the speckle observation so we plot both possibilities.

WSB 59 was resolved as a binary with a separation of 100 mas at a position angle of  $103^\circ$  through speckle observations by Ratzka et al. (2005). We resolved the binary during three of our AO observations in 2014–2015, most recently with a separation of 73 mas at a position angle of  $267^\circ$ . This suggests a large change in position over the past 15 years. Ratzka et al. (2005) do not mention explicitly an ambiguity in the position angle of the speckle observations of WSB 59, although the measured separation is near their resolution limit so they could not distinguish between an elongated structure and a

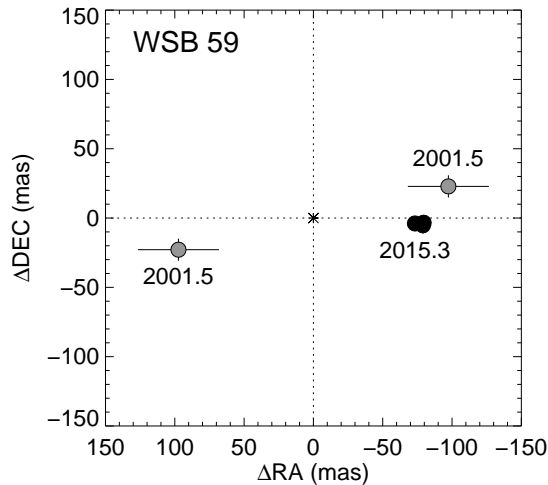


**Figure 22.** Orbital motion measured for the close pair in WSB 59 based on our AO observations (black circle) and the speckle measurement (gray circle) from Ratzka et al. (2005). The published position angle of the speckle measurement is almost  $180^\circ$  different from the most recent AO observations. Ratzka et al. (2005) do not mention explicitly an ambiguity in the position angle but their measurement was near the resolution limit, so we include the flipped position angle in the plot as an alternate possibility.

binary star. If we flip the position angle of that measurement by  $180^\circ$ , then the change in position is much smaller. Figure 22 shows both possibilities. Additional measurements along the orbit would clarify the direction of motion. The  $K$ -band flux ratio of WSB 59 is twice as large compared with the initial measurement by Ratzka et al. (2005).

#### 4. CONCLUSIONS

We present recent measurements of the orbital positions of 17 multiple systems in the Ophiuchus star forming region and the UCL cluster based on AO imaging at the Keck Observatory. We detected visual companions of MML 50 and MML 53 for the first time and report the possible detection of a close third companion in WSB 21 and V853 Oph. We did not resolve EM\* SR 20 during our AO observations, but present a preliminary orbit based on previously published measurements. We also provide a preliminary orbit for EM\* SR 24N and a revised visual orbit for the close pair in ROXs 47A based on additional AO measurements reported in this paper. Most of the observed binaries do not have enough orbital measurements to determine a preliminary orbital solution, however, the positions reported here will help to plan the frequency of future observations and provide data for the eventual determination of the orbital solutions and dynamical masses.

We thank the staff at the Keck Observatory for their support during our NIRC2 observing runs. We thank the referee for providing feedback that improved the paper. GHS acknowledges support from NASA Keck PI Data Awards administered by the NASA Exoplanet Science Institute and from NSF Grant AST-1411654. Data presented herein were obtained at the W. M. Keck Observatory from telescope time allocated to the National Aeronautics and Space Administration through the agency’s scientific partnership with the California Institute of Technology and the University of California. The Observatory was made possible by the generous financial support of the W. M. Keck Foundation. We recognize and acknowledge the significant cultural role that the summit of Mauna Kea plays within the indigenous Hawaiian community and are grateful for the opportunity to conduct these observations from the mountain. This research has made use of the SIMBAD database and the VizieR catalog access tool, CDS, Strasbourg, France.

#### REFERENCES

- Ageorges, N., Eckart, A., Monin, J.-L., & Menard, F. 1997, *A&A*, 326, 632
- Allen, L. E., Myers, P. C., Di Francesco, J., et al. 2002, *ApJ*, 566, 993
- Andrews, S. M., & Williams, J. P. 2005, *ApJL*, 619, L175
- Aspin, C., Puxley, P. J., Hawarden, T. G., Paterson, M. J., & Pickup, D. A. 1997, *MNRAS*, 284, 257
- Baraffe, I., Homeier, D., Allard, F., & Chabrier, G. 2015, *A&A*, 577, A42
- Barsony, M., Koresko, C., & Matthews, K. 2003, *ApJ*, 591, 1064
- Barton, S. G. 1951, *AJ*, 55, 218
- Beck, T. L., Schaefer, G. H., Simon, M., et al. 2004, *ApJ*, 614, 235
- Boden, A. F., Sargent, A. I., Akeson, R. L., et al. 2005, *ApJ*, 635, 442
- Bouvier, J., & Appenzeller, I. 1992, *A&AS*, 92, 481
- Bowler, B. P., Liu, M. C., Kraus, A. L., & Mann, A. W. 2014, *ApJ*, 784, 65
- Burnham, K. P., & Anderson, D. R. 2002, *Model Selection and Multimodel Inference: A Practical Information-Theoretic Approach* (New York: Springer-Verlag)
- Cheetham, A. C., Kraus, A. L., Ireland, M. J., et al. 2015, *ApJ*, 813, 83
- Cieza, L. A., Schreiber, M. R., Romero, G. A., et al. 2010, *ApJ*, 712, 925
- Correia, S., Zinnecker, H., Ratzka, T., & Sterzik, M. F. 2006, *A&A*, 459, 909

- Costa, A., Jessop, N. E., Yun, J. L., et al. 2000, in IAU Symposium, Vol. 200, IAU Symposium, 48
- de Zeeuw, P. T., Hoogerwerf, R., de Bruijne, J. H. J., Brown, A. G. A., & Blaauw, A. 1999, *AJ*, 117, 354
- Duchêne, G., Beust, H., Adjali, F., Konopacky, Q. M., & Ghez, A. M. 2006, *A&A*, 457, L9
- Duchêne, G., & Kraus, A. 2013, *ARA&A*, 51, 269
- Erickson, K. L., Wilking, B. A., Meyer, M. R., Robinson, J. G., & Stephenson, L. N. 2011, *AJ*, 142, 140
- Feiden, G. A. 2016, *A&A*, 593, A99
- Fekel, Jr., F. C. 1981, *ApJ*, 246, 879
- Fernández-López, M., Zapata, L. A., & Gabbasov, R. 2017, *ApJ*, 845, 10
- Gaia Collaboration, Prusti, T., de Bruijne, J. H. J., et al. 2016, *A&A*, 595, A1
- Geoffray, H., & Monin, J.-L. 2001, *A&A*, 369, 239
- Ghez, A. M., Neugebauer, G., & Matthews, K. 1993, *AJ*, 106, 2005
- Ghez, A. M., Weinberger, A. J., Neugebauer, G., Matthews, K., & McCarthy, Jr., D. W. 1995, *AJ*, 110, 753
- Greene, T. P., Wilking, B. A., Andre, P., Young, E. T., & Lada, C. J. 1994, *ApJ*, 434, 614
- Hebb, L., Cegla, H. M., Stassun, K. G., et al. 2011, *A&A*, 531, A61
- Hebb, L., Stempels, H. C., Aigrain, S., et al. 2010, *A&A*, 522, A37
- Heintz, W. D. 1980, *ApJS*, 44, 111
- Kellogg, K., Prato, L., Torres, G., et al. 2017, *ApJ*, 844, 168
- Köhler, R., Kasper, M., Herbst, T. M., Ratzka, T., & Bertrang, G. H.-M. 2016, *A&A*, 587, A35
- Köhler, R., Ratzka, T., Petr-Gotzens, M. G., & Correia, S. 2013, *A&A*, 558, A80
- Koresko, C. D. 2002, *AJ*, 124, 1082
- Kraus, A. L., & Hillenbrand, L. A. 2007, *AJ*, 134, 2340
- Kuzuhara, M., Tamura, M., Ishii, M., et al. 2011, *AJ*, 141, 119
- Le Bouquin, J.-B., Monin, J.-L., Berger, J.-P., et al. 2014, *A&A*, 561, A101
- Luhman, K. L., Stauffer, J. R., Muench, A. A., et al. 2003, *ApJ*, 593, 1093
- Mamajek, E. E. 2008, *Astronomische Nachrichten*, 329, 10
- Mamajek, E. E., Meyer, M. R., & Liebert, J. 2002, *AJ*, 124, 1670
- Martin, E. L., Montmerle, T., Gregorio-Hetem, J., & Casanova, S. 1998, *MNRAS*, 300, 733
- Mathieu, R. D., Walter, F. M., & Myers, P. C. 1989, *AJ*, 98, 987
- McCabe, C., Ghez, A. M., Prato, L., et al. 2006, *ApJ*, 636, 932
- Ortiz-León, G. N., Loinard, L., Kounkel, M. A., et al. 2017, *ApJ*, 834, 141
- Paxton, B., Bildsten, L., Dotter, A., et al. 2011, *ApJS*, 192, 3
- Pinilla, P., Pérez, L. M., Andrews, S., et al. 2017, *ApJ*, 839, 99
- Prato, L., & Simon, M. 1997, *ApJ*, 474, 455
- Ratzka, T., Köhler, R., & Leinert, C. 2005, *A&A*, 437, 611
- Reipurth, B., Clarke, C. J., Boss, A. P., et al. 2014, *Protostars and Planets VI*, 267
- Reipurth, B., & Zinnecker, H. 1993, *A&A*, 278, 81
- Richichi, A., Leinert, C., Jameson, R., & Zinnecker, H. 1994, *A&A*, 287, 145
- Rizzuto, A. C., Ireland, M. J., Dupuy, T. J., & Kraus, A. L. 2016, *ApJ*, 817, 164
- Schaefer, G. H., Prato, L., Simon, M., & Patience, J. 2014, *AJ*, 147, 157
- Schaefer, G. H., Prato, L., Simon, M., & Zavala, R. T. 2012, *ApJ*, 756, 120
- Schaefer, G. H., Simon, M., Beck, T. L., Nelan, E., & Prato, L. 2006, *AJ*, 132, 2618
- Service, M., Lu, J. R., Campbell, R., et al. 2016, *PASP*, 128, 095004
- Simon, M., Howell, R. R., Longmore, A. J., et al. 1987, *ApJ*, 320, 344
- Simon, M., Schaefer, G. H., Prato, L., et al. 2013, *ApJ*, 773, 28
- Simon, M., Ghez, A. M., Leinert, C., et al. 1995, *ApJ*, 443, 625
- Simon, M., Guilloteau, S., Di Folco, E., et al. 2017, *ApJ*, 844, 158
- Sterzik, M. F., & Tokovinin, A. A. 2002, *A&A*, 384, 1030
- Struve, O., & Rudkjøbing, M. 1949, *ApJ*, 109, 92
- Tokovinin, A. 2014, *AJ*, 147, 87
- Torres, C. A. O., Quast, G. R., da Silva, L., et al. 2006, *A&A*, 460, 695
- Torres, G., Ruíz-Rodríguez, D., Badenas, M., et al. 2013, *ApJ*, 773, 40
- Torres, R. M., Loinard, L., Mioduszewski, A. J., et al. 2012, *ApJ*, 747, 18
- White, R. J., Gabor, J. M., & Hillenbrand, L. A. 2007, *AJ*, 133, 2524
- Wichmann, R., Sterzik, M., Krautter, J., Metanomski, A., & Voges, W. 1997, *A&A*, 326, 211
- Wilking, B. A., Meyer, M. R., Robinson, J. G., & Greene, T. P. 2005, *AJ*, 130, 1733
- Wizinowich, P. L., Acton, D. S., Lai, O., et al. 2000, *Proc. SPIE*, 4007, 2
- Yelda, S., Lu, J. R., Ghez, A. M., et al. 2010, *ApJ*, 725, 331
- Zinnecker, H., & Perrier, C. 1988, *The Messenger*, 51, 31

**Table 1.** Observed Multiple Systems

Name	RA (2000)	DEC (2000)	Distance (pc)	Region	SpT	References
MML 50	14 50 25.814	-35 06 48.60	140	UCL	K0	S1, D1
MML 53	14 58 37.697	-35 40 30.44	140	UCL	K2	S1, D1
WSB 18	16 24 59.741	-24 56 00.83	130	Oph	M3.5	S2, D2
WSB 21	16 25 15.22	-25 11 54.1	130	Oph	M5	S3, D2
ROX 1-SR 2	16 25 19.244	-24 26 52.68	130	Oph	G9	S4, D2
ROXs 5	16 25 55.825	-23 55 09.97	130	Oph	K7	S5, D2
ROXR1 12	16 26 01.61	-24 29 45.0	137.3	L 1688	M3	S6, D3
WSB 37	16 26 41.257	-24 40 17.96	137.3	L 1688	M5	S6, D3
ROXs 16	16 26 46.43	-24 12 00.1	137.3	L 1688	G3.5	S6, D3
WSB 41 (SR 24N)	16 26 58.44	-24 45 31.9	137.3	L 1688	K8	S7, D3
HBC 263 (SR 12)	16 27 19.512	-24 41 40.39	137.3	L 1688	M0	S6, D3
VSSG 14	16 27 49.87	-24 25 40.2	137.3	L 1688	A7	S6, D3
WSB 59	16 28 09.209	-23 52 20.51	137.3	Oph	M0	S3, D3
HBC 643 (SR 20)	16 28 32.66	-24 22 44.9	130	Oph	G7	S6, D2
V853 Oph	16 28 45.28	-24 28 19.0	130	Oph	M3.75	S6, D2
ROXs 42C	16 31 15.745	-24 34 02.23	147.3	L 1689	K6	S8, D3
ROXs 43A	16 31 20.120	-24 30 05.08	147.3	L 1689	G0	S5, D3
ROXs 43B	16 31 20.195	-24 30 00.91	147.3	L 1689	K5	S5, D3
ROXs 47A (DoAr51)	16 32 11.794	-24 40 21.37	143.2	L 1689	K3	S5, D3

**References**—Spectral Types: S1 - [Mamajek et al. \(2002\)](#); S2 - [Erickson et al. \(2011\)](#); S3 - Prato et al. in prep; S4 - [Torres et al. \(2006\)](#); S5 - [Bouvier & Appenzeller \(1992\)](#); S6 - [Wilking et al. \(2005\)](#); S7 - [Luhman et al. \(2003\)](#); S8 - [Cieza et al. \(2010\)](#); Distances: D1 - [de Zeeuw et al. \(1999\)](#); D2 - [Cheetham et al. \(2015\)](#); D3 - [Ortiz-León et al. \(2017\)](#)

Table 2. Log of Keck NIRC2 AO Observations

UT Date	UT	Target	Filter	AO Rate	$T_{\text{int}}$ (s) <sup>a</sup>	No. Images <sup>b</sup>	PSF Used
2004 Jul 14	09:15	ROXs 47A	$H, K'$	50	0.18	10, 10	faint wide comp
2014 Jul 05	06:36	MML 53	$K'$	149	4.0	30	ROXs 47B
	07:01	ROX 1 - SR2	$J, H, K'$	149	1.0–2.0	6, 12, 12	ePSF
	07:24	ROXs 47B	$J, H, K'$	60	1.0–2.0	6, 12, 12	Single PSF
	07:43	ROXs 42C	$J, H, K'$	149	0.2–1.0	6, 12, 12	primary
	08:02	ROXs 5	$J, H, K', L'$	149	0.18–1.0	6, 12, 12, 6	ePSF
	08:23	ROXs 3	$J, H, K', L'$	149	0.18	6, 6, 6, 6	Single PSF
	08:37	WSB 59	$K'$	149	1.0	6	ePSF
	08:51	VSSG 14	$H, K'$	60	0.5	6, 6	ROXs 3
	09:46	HBC 263 - SR 12	$H, K'$	149	1.0, 0.5	12, 12	ePSF
		HBC 263 - SR 12	$H$	438	0.5	6	ePSF
2014 Jul 06	08:08	HBC 643 - SR 20	Hcont, Kcont	250	0.5–1.0	12, 12	Haro 1-16
	08:31	Haro 1-16	Hcont, Kcont	250	1.0	6, 6	Single PSF
	08:45	VSSG 14	Hcont, Kcont	149	0.5	12, 12	ROXs 10A
	08:57	ROXs 10A	Hcont, Kcont	148	0.5	6, 6	Single PSF
	09:07	WSB 59	Kcont	60	1.0–2.0	12	ePSF
	09:20	ROXs 16	$K'$	60	0.5	12	Tertiary
	09:28	ROXs 47A	$K'$	149	0.5	12	Tertiary
	09:38	WSB 41 - SR 24N	Kcont	60	0.5	12	SR 24S
	09:49	V853 Oph	$H, \text{Hcont}, \text{Kcont}$	250	0.2–1.0	6, 6, 6	Tertiary
2015 Apr 05	11:01	MML 53	Jcont, Hcont, Kcont, $L'$	438	0.18–1.0	6, 12, 12, 6	MML 50 A
	11:22	MML 50	Jcont, Hcont, Kcont, $L'$	438	0.18–1.0	6, 6, 6, 6	Primary
	11:41	WSB 18	$J, H, K', L'$	440	0.18–1.0	6, 12, 12, 6	Wide component
	12:09	ROXs 16	Jcont, Hcont, Kcont, $L'$	440	0.18–1.0	6, 12, 12, 6	Faint tertiary
	12:34	WSB 21	$J, H, K', L'$	440	0.18–0.5	6, 12, 12, 6	Primary
	12:52	ROXs 20A	$J, H, K', L'$	440	0.18–0.5	6, 6, 6, 6	Single PSF
	13:10	WSB 37	$J, H, K', L'$	440	0.18–0.5	6, 12, 12, 6	ePSF
	13:40	WSB 59	$J, H, K', L'$	750	0.18–0.5	6, 12, 12, 6	ePSF
	13:59	ROXs 20A	$J, H, K', L'$	750	0.18–0.5	6, 12, 6, 6	Single PSF
	14:18	ROXR1 12	$J, H, K', L'$	750	0.18–0.5	6, 12, 12, 6	ePSF
	14:40	VSSG 14	Jcont, Hcont, Kcont, $L'$	750	0.18–2.0	6, 12, 12, 6	ROXs 20B
	14:59	ROXs 20B	Jcont, Hcont, Kcont, $L'$	750	0.18–2.0	6, 6, 6, 6	Single PSF
	15:12	V853 Oph	Jcont, Hcont, Kcont, $L'$	750	0.18–0.5	6, 12, 12, 6	Tertiary
	15:29	ROXs 47A	$J, H, \text{Kcont}, L'$	750	0.18–0.5	6, 12, 12, 6	Tertiary
2015 Jul 12	05:46	MML 53	Hcont, Kcont	438	0.5–1.0	12, 12	MML 50 A
	05:59	MML 50	Hcont, Kcont	438	0.5–0.7	6, 6	MML 50 A
	06:13	ROXs 43 A	Jcont, Hcont, Kcont, $L'$	438	0.18–0.6	10, 10, 10, 20	ROXs 43 Aa
	07:33	ROXs 5	Jcont, Hcont, Kcont, $L'$	250	0.18–1.5	6, 6, 6, 6	ePSF
	07:50	ROXs 3	Jcont, Hcont, Kcont, $L'$	250	0.18–1.0	6, 6, 6, 6	Single PSF
	08:05	HBC 263 - SR 12	Jcont, Hcont, Kcont, $L'$	250	0.18–1.0	6, 6, 6, 6	ePSF
	08:21	ROXs 42C	Jcont, Hcont, Kcont, $L'$	438	0.18–0.5	6, 6, 6, 6	Primary
	08:37	V853 Oph	Hcont, Kcont	250	0.5–0.8	12, 12	Wide faint comp
	08:47	ROX 1 - SR 2	Jcont, Hcont, Kcont, $L'$	438	0.18–0.8	6, 6, 6, 6	ePSF
	09:00	ROXs 47B	Jcont, Hcont, Kcont, $L'$	438	0.18–1.0	3, 3, 6, 3	Single PSF
	09:16	WSB 41 - SR 24N	Jcont, Hcont, Kcont, $L'$	149	0.18–0.5	10, 10, 10, 10	SR 24S
	09:30	ROXs 47A	Hcont, Kcont	250	0.5	5, 5	Faint tertiary

Table 2 continued



Table 2 (*continued*)

UT Date	UT	Target	Filter	AO Rate	$T_{\text{int}}$ (s) <sup>a</sup>	No. Images <sup>b</sup>	PSF Used
---------	----	--------	--------	---------	-----------------------------------	-------------------------	----------

<sup>a</sup> Integration time per co-add. Each image is composed of 10 co-added exposures. If different exposure times were used for different sets of images, then the range of values is listed.

<sup>b</sup> The number of images taken in each filter.

**Table 3.** Keck NIRC2 Adaptive Optics Measurements of the Orbital Positions in Multiple Systems<sup>a</sup>

Julian Year	$\rho$ (mas)	P.A.( $^{\circ}$ )	Filter	Flux Ratio
MML 50				
2015.2580	$375.58 \pm 0.66$	$20.906 \pm 0.101$	Jcont	$0.0919 \pm 0.0039$
			Hcont	$0.1029 \pm 0.0010$
			Kcont	$0.1266 \pm 0.0038$
			Lcont	$0.1427 \pm 0.0025$
2015.5257	$375.59 \pm 0.28$	$21.043 \pm 0.044$	Hcont	$0.1038 \pm 0.0016$
			Kcont	$0.1267 \pm 0.0013$
MML 53				
2014.5073	$57.07 \pm 2.46$	$19.16 \pm 2.47$	$K'$	$0.530 \pm 0.116$
2015.2579	$53.67 \pm 1.93$	$28.34 \pm 2.06$	Jcont	$0.429 \pm 0.045$
			Hcont	$0.416 \pm 0.030$
			Kcont	$0.389 \pm 0.020$
			$L'$	$0.370 \pm 0.035$
2015.5256	$50.58 \pm 1.30$	$36.49 \pm 1.48$	Hcont	$0.359 \pm 0.016$
			Kcont	$0.403 \pm 0.017$
ROX 1 - EM* SR 2				
2014.5073	$153.69 \pm 2.08$	$125.507 \pm 0.774$	$J$	$1.064 \pm 0.131$
			$H$	$1.005 \pm 0.016$
			$K'$	$1.010 \pm 0.044$
2015.5260	$149.50 \pm 0.13$	$123.474 \pm 0.054$	Jcont	$0.9720 \pm 0.0031$
			Hcont	$0.9639 \pm 0.0021$
			Kcont	$0.9624 \pm 0.0020$
			$L'$	$0.9568 \pm 0.0033$
ROXR1 12				
2015.2583	$107.04 \pm 0.52$	$9.99 \pm 0.28$	$J$	$0.8218 \pm 0.0279$
			$H$	$0.7837 \pm 0.0075$
			$K'$	$0.8031 \pm 0.0050$
			$L'$	$0.8466 \pm 0.0179$
ROXs 5				
2014.5074	$184.07 \pm 0.35$	$351.40 \pm 0.11$	$J$	$0.3921 \pm 0.0070$
			$H$	$0.4309 \pm 0.0044$
			$K'$	$0.4387 \pm 0.0072$

*Table 3 continued*

Table 3 (*continued*)

Julian Year	$\rho(\text{mas})$	P.A.( $^{\circ}$ )	Filter	Flux Ratio
2015.5258	$180.43 \pm 0.34$	$352.96 \pm 0.11$	$L'$	$0.4490 \pm 0.0220$
			Jcont	$0.3845 \pm 0.0087$
			Hcont	$0.4200 \pm 0.0049$
			Kcont	$0.4435 \pm 0.0037$
			$L'$	$0.4616 \pm 0.0033$
ROXs 16 A,B				
2014.5103	$545.99 \pm 0.35$	$114.017 \pm 0.037$	$K'$	$0.1915 \pm 0.0011$
2015.2581	$543.05 \pm 0.71$	$114.093 \pm 0.076$	Jcont	$0.2670 \pm 0.0218$
			Hcont	$0.2152 \pm 0.0042$
			Kcont	$0.1572 \pm 0.0023$
			$L'$	$0.0884 \pm 0.0009$
ROXs 42C				
2014.5074	$350.29 \pm 0.34$	$160.414 \pm 0.056$	$J$	$0.2515 \pm 0.0028$
			$H$	$0.2640 \pm 0.0038$
			$K'$	$0.2554 \pm 0.0028$
2015.5259	$353.58 \pm 0.31$	$160.855 \pm 0.053$	Jcont	$0.2460 \pm 0.0031$
			Hcont	$0.2534 \pm 0.0018$
			Kcont	$0.2603 \pm 0.0012$
			$L'$	$0.2455 \pm 0.0020$
ROXs 43 Aa,Ab				
2015.5257	$299.61 \pm 0.75$	$159.07 \pm 0.14$	Jcont	$0.0335 \pm 0.0016$
			Hcont	$0.0394 \pm 0.0012$
			Kcont	$0.0402 \pm 0.0009$
			$L'$	$0.0470 \pm 0.0014$
ROXs 43 Aa,B				
2015.5257	$4479.6 \pm 1.2$	$11.880 \pm 0.025$	Jcont	$0.595 \pm 0.029$
			Hcont	$0.625 \pm 0.024$
			Kcont	$0.538 \pm 0.011$
			$L'$	$0.364 \pm 0.018$
ROXs 47 Aa,Ab				
2004.5336	$25.67 \pm 2.60$	$38.08 \pm 5.80$	$H$	$1.166 \pm 0.309$
			$K'$	$1.159 \pm 0.408$
2014.5103	$51.95 \pm 0.73$	$72.90 \pm 0.81$	$K'$	$0.896 \pm 0.012$
			$J$	$0.858 \pm 0.052$
2015.2584	$55.68 \pm 4.61$	$80.04 \pm 4.75$	$H$	$0.834 \pm 0.080$
			Kcont	$0.807 \pm 0.097$
			$L'$	$0.912 \pm 0.022$
			Hcont	$0.967 \pm 0.037$
2015.5261	$56.92 \pm 0.60$	$82.01 \pm 0.61$	Kcont	$0.979 \pm 0.008$
ROXs 47 Ac,Aa				

*Table 3 continued*

Table 3 (*continued*)

Julian Year	$\rho(\text{mas})$	P.A.( $^\circ$ )	Filter	Flux Ratio
2004.5336	$796.57 \pm 2.26$	$260.205 \pm 0.163$	<i>H</i>	$3.404 \pm 0.463$
			<i>K'</i>	$2.475 \pm 0.478$
2014.5103	$815.57 \pm 0.55$	$264.554 \pm 0.040$	<i>K'</i>	$3.340 \pm 0.036$
2015.2584	$818.04 \pm 4.35$	$265.040 \pm 0.305$	<i>J</i>	$2.665 \pm 0.205$
			<i>H</i>	$2.403 \pm 0.142$
			Kcont	$1.685 \pm 0.093$
			<i>L'</i>	$1.106 \pm 0.015$
2015.5261	$820.21 \pm 1.00$	$265.172 \pm 0.073$	Hcont	$2.484 \pm 0.107$
			Kcont	$1.646 \pm 0.026$
ROXs 47 Ac,Ab				
2004.5336	$777.72 \pm 2.75$	$261.474 \pm 0.203$	<i>H</i>	$3.843 \pm 0.532$
			<i>K'</i>	$2.697 \pm 0.502$
2014.5103	$764.76 \pm 0.49$	$265.341 \pm 0.038$	<i>K'</i>	$2.993 \pm 0.025$
2015.2584	$762.58 \pm 3.82$	$265.405 \pm 0.287$	<i>J</i>	$2.279 \pm 0.098$
			<i>H</i>	$1.993 \pm 0.070$
			Kcont	$1.354 \pm 0.121$
			<i>L'</i>	$1.008 \pm 0.012$
2015.5261	$763.38 \pm 1.10$	$265.408 \pm 0.085$	Hcont	$2.398 \pm 0.043$
			Kcont	$1.611 \pm 0.018$
EM* SR 12 (HBC 263)				
2014.5076	$171.80 \pm 0.22$	$79.669 \pm 0.074$	<i>H</i>	$0.9373 \pm 0.0078$
			<i>K'</i>	$0.9357 \pm 0.0049$
2015.5259	$164.62 \pm 0.17$	$79.326 \pm 0.062$	Jcont	$0.9506 \pm 0.0060$
			Hcont	$0.9699 \pm 0.0055$
			Kcont	$0.9502 \pm 0.0054$
			<i>L'</i>	$0.9414 \pm 0.0049$
EM* SR 24 Na,Nb (WSB 41)				
2014.5103	$93.73 \pm 1.58$	$248.03 \pm 0.97$	Kcont	$0.461 \pm 0.023$
2015.5260	$99.11 \pm 0.29$	$240.68 \pm 0.17$	Jcont	$0.973 \pm 0.030$
			Hcont	$0.992 \pm 0.020$
			Kcont	$1.059 \pm 0.017$
			<i>L'</i>	$1.091 \pm 0.008$
EM* SR 24 S,Na				
2014.5103	$5071.40 \pm 10.28$	$349.48 \pm 0.12$	Kcont	$0.585 \pm 0.041$
2015.5260	$5070.38 \pm 8.94$	$349.48 \pm 0.10$	Jcont	$0.504 \pm 0.024$
			Hcont	$0.470 \pm 0.021$
			Kcont	$0.464 \pm 0.014$
			<i>L'</i>	$0.519 \pm 0.036$
EM* SR 24 S,Nb				
2014.5103	$5053.63 \pm 9.85$	$348.44 \pm 0.11$	Kcont	$0.270 \pm 0.026$
2015.5260	$5039.31 \pm 9.02$	$348.42 \pm 0.10$	Jcont	$0.490 \pm 0.020$
			Hcont	$0.467 \pm 0.027$
			Kcont	$0.492 \pm 0.019$

Table 3 continued

Table 3 (*continued*)

Julian Year	$\rho(\text{mas})$	P.A.( $^\circ$ )	Filter	Flux Ratio
			$L'$	$0.567 \pm 0.043$
V853 Oph B,A				
2003.2855	$345.37 \pm 1.85$	$273.901 \pm 0.307$	$H$	$2.945 \pm 0.064$
			$K'$	$3.484 \pm 0.105$
2004.5335	$337.81 \pm 0.39$	$272.811 \pm 0.066$	$H$	$2.823 \pm 0.039$
			$K'$	$3.362 \pm 0.056$
2014.5104	$272.34 \pm 0.52$	$269.209 \pm 0.109$	$H$	$3.305 \pm 0.043$
			Hcont	$3.219 \pm 0.061$
			Kcont	$3.634 \pm 0.034$
2015.2584	$265.67 \pm 0.62$	$268.744 \pm 0.135$	Jcont	$2.498 \pm 0.471$
			Hcont	$3.457 \pm 0.327$
			Kcont	$4.312 \pm 0.057$
			$L'$	$5.527 \pm 0.138$
2015.5260	$265.26 \pm 0.12$	$268.723 \pm 0.032$	Kcont	$5.109 \pm 0.018$
			Hcont	$4.136 \pm 0.023$
V853 Oph B,Aa - possible triple fit				
2014.5104	$276.95 \pm 1.00$	$271.09 \pm 0.21$	$H$	$1.943 \pm 0.033$
			Hcont	$1.992 \pm 0.044$
			Kcont	$2.297 \pm 0.080$
V853 Oph B,Ab - possible triple fit				
2014.5104	$265.69 \pm 0.60$	$266.73 \pm 0.13$	$H$	$1.591 \pm 0.058$
			Hcont	$1.505 \pm 0.149$
			Kcont	$1.679 \pm 0.093$
V853 Oph Aa,Ab - possible triple fit				
2014.5104	$23.51 \pm 0.97$	$150.34 \pm 2.36$	$H$	$0.819 \pm 0.036$
			Hcont	$0.757 \pm 0.091$
			Kcont	$0.733 \pm 0.064$
VSSG 14				
2014.5075 <sup>b</sup>	$63.77 \pm 2.22$	$220.34 \pm 1.99$	$K'$	$0.415 \pm 0.035$
2014.5102	$70.62 \pm 1.63$	$220.68 \pm 1.32$	Hcont	$0.286 \pm 0.022$
			Kcont	$0.365 \pm 0.010$
2015.2583	$67.85 \pm 2.93$	$206.99 \pm 2.47$	Jcont	$0.163 \pm 0.037$
			Hcont	$0.240 \pm 0.032$
			Kcont	$0.338 \pm 0.044$
			$L'$	$0.377 \pm 0.013$
WSB 18 Aa,Ab				
2015.2580	$68.69 \pm 0.72$	$14.28 \pm 0.60$	$J$	$0.554 \pm 0.024$
			$H$	$0.506 \pm 0.021$
			$K'$	$0.511 \pm 0.008$
			$L'$	$0.539 \pm 0.047$

*Table 3 continued*

Table 3 (*continued*)

Julian Year	$\rho(\text{mas})$	P.A.( $^\circ$ )	Filter	Flux Ratio
WSB 18 B,Aa				
2015.2580	$1097.41 \pm 0.92$	$259.324 \pm 0.049$	<i>J</i>	$1.184 \pm 0.031$
			<i>H</i>	$1.178 \pm 0.043$
			<i>K'</i>	$0.968 \pm 0.016$
			<i>L'</i>	$0.631 \pm 0.020$
WSB 18 B,Ab				
2015.2580	$1070.23 \pm 0.97$	$262.659 \pm 0.053$	<i>J</i>	$0.655 \pm 0.021$
			<i>H</i>	$0.596 \pm 0.013$
			<i>K'</i>	$0.495 \pm 0.011$
			<i>L'</i>	$0.339 \pm 0.022$
WSB 21 A,B - binary fit				
2015.2581	$202.04 \pm 0.36$	$76.33 \pm 0.10$	<i>J</i>	$0.8918 \pm 0.0092$
			<i>H</i>	$0.8037 \pm 0.0057$
			<i>K'</i>	$0.7721 \pm 0.0026$
			<i>L'</i>	$0.6772 \pm 0.0131$
WSB 21 Ba,Bb - possible triple fit				
2015.2581	$21.47 \pm 0.80$	$164.09 \pm 2.15$	<i>J</i>	$0.74 \pm 0.12$
			<i>H</i>	$0.73 \pm 0.10$
			<i>K'</i>	$0.72 \pm 0.10$
			<i>L'</i>	$0.50 \pm 0.15$
WSB 21 A,Ba - possible triple fit				
2015.2581	$201.99 \pm 0.67$	$73.84 \pm 0.19$	<i>J</i>	$0.534 \pm 0.038$
			<i>H</i>	$0.486 \pm 0.029$
			<i>K'</i>	$0.474 \pm 0.027$
			<i>L'</i>	$0.474 \pm 0.048$
WSB 21 A,Bb - possible triple fit				
2015.2581	$203.03 \pm 1.00$	$79.91 \pm 0.28$	<i>J</i>	$0.391 \pm 0.035$
			<i>H</i>	$0.352 \pm 0.030$
			<i>K'</i>	$0.341 \pm 0.025$
			<i>L'</i>	$0.232 \pm 0.048$
WSB 37				
2015.2582	$117.65 \pm 0.16$	$254.354 \pm 0.079$	<i>J</i>	$1.0223 \pm 0.0124$
			<i>H</i>	$0.9917 \pm 0.0030$
			<i>K'</i>	$0.9773 \pm 0.0034$
			<i>L'</i>	$0.9755 \pm 0.0086$
WSB 59				
2014.5075	$79.17 \pm 5.98$	$266.21 \pm 4.33$	<i>K'</i>	$0.566 \pm 0.062$

*Table 3 continued*

Table 3 (*continued*)

Julian Year	$\rho$ (mas)	P.A.( $^\circ$ )	Filter	Flux Ratio
2014.5103	$79.59 \pm 3.01$	$267.56 \pm 2.17$	Kcont	$0.596 \pm 0.041$
2015.2582	$73.36 \pm 0.51$	$266.94 \pm 0.40$	<i>J</i>	$0.476 \pm 0.013$
			<i>H</i>	$0.505 \pm 0.009$
			<i>K'</i>	$0.564 \pm 0.007$
			<i>L'</i>	$0.648 \pm 0.018$

<sup>a</sup>When listed, the “X,Y” designation indicates that component Y was measured relative to X.

<sup>b</sup>*H*-band images of VSSG 14 from UT 2014 Jul 5 (2014.5075) were of poor quality and not included in the final results. The discrepancy between the two positions measured in 2014.5 is likely because of a larger mismatch of PSF shapes on UT 2014 Jul 5. The components of VSSG 14 were too blended to create an effective PSF.

NOTE—ROX 47 Ac,Aa and Ac,Ab give the position angle of the brighter component relative to the fainter tertiary. This angle is flipped  $180^\circ$  from the position angle given in the literature for the faint companion relative to the brighter primary.

Table 4. Orbital Parameters

Parameters	ROXs 47A	EM* SR 20	EM* SR 24 N
<i>P</i> (yr)	$8.051 \pm 0.039$	$23.2^{+1.1}_{-0.9}$	$111^{+105}_{-33}$
<i>T</i> (JY)	$2012.035 \pm 0.035$	$2002.6^{+7.7}_{-5.4}$	$2009.34^{+0.15}_{-0.13}$
<i>e</i>	$0.7961 \pm 0.0062$	$0.26^{+0.73}_{-0.11}$	$0.64^{+0.13}_{-0.10}$
<i>a</i> (mas)	$32.76 \pm 0.48$	$48^{+420}_{-6}$	$181^{+83}_{-30}$
<i>i</i> ( $^\circ$ )	$20.7 \pm 4.6$	$130^{+21}_{-37}$	$132.1^{+7.4}_{-5.0}$
$\Omega$ ( $^\circ$ )	$51.4 \pm 8.5$	$90^{+43}_{-13}$	$72.0^{+4.3}_{-3.4}$
$\omega$ ( $^\circ$ )	$216.9 \pm 9.0$	$67^{+41}_{-46}$	$110.9^{+5.0}_{-5.8}$
$M_{\text{tot}}$ ( $M_\odot$ )	$1.593 \pm 0.079$	$0.7^{+1.2}_{-0.3} \left(\frac{d}{130\text{pc}}\right)^3$	$1.24^{+0.24}_{-0.23} \left(\frac{d}{137.3\text{pc}}\right)^3$

NOTE—The total mass of ROXs 47A includes the uncertainty in the orbital parallax ( $143.2 \pm 1.0$  pc) determined by [Ortiz-León et al. \(2017\)](#). The total mass of SR 20 is the median from a statistical analysis of orbits that fit the data; the uncertainties contain 34% of the solutions on either side of the median. The total mass of SR 24 N was determined from the  $1\sigma$  ( $\Delta\chi^2 = 1$ ) confidence interval. The uncertainties in the masses for SR 20 and SR 24 are derived from the visual orbit only and do not include uncertainties in the distance. The distances for these systems are not yet precisely known and will be refined by astrometric missions like GAIA.